ZEUS-NOTE 98-XXX

February 1, 1998

# Measurement of Elastic $\Upsilon$, $\psi'$ and $J/\psi$ Photoproduction at HERA

*R. Brugnera, S. Limentani, Padova University*

**Abstract**

The reactions $e^+p \to e^+p\,\Upsilon$, $e^+p \to e^+p\,\psi'$ and $e^+p \to e^+p\,J/\psi$ have been studied using the ZEUS detector at HERA at a median photon virtuality $Q^2$ of $5 \times 10^{-5}$ GeV$^2$ and for photon-proton centre of mass energies in the range $80 < W < 280$ GeV for the $\Upsilon$ and $40 < W < 160$ GeV for the $\psi'$ and $J/\psi$. The $\Upsilon$ , $\psi'$ and $J/\psi$ were detected via their decay into a couple of muons.

## 1 Introduction

In this note we present an analysis of elastic $\Upsilon$, $\psi'$ and $J/\psi$ photo-production in positron proton scattering using the ZEUS detector at HERA. The vector mesons are detected in their muonic decay mode. In order to restrict the analysis to the elastic photoproduction, the detector is required to be empty except for the decay products. The data presented below correspond to 43 pb$^{-1}$ of data collected in the 1995+96+97 HERA data taking periods.

The interest in elastic vector meson ($V$) photoproduction is two fold: first, it provides a testing ground for QCD descriptions of the pomeron and, second, in the context of specific models, it allows the extraction of the gluon density of the proton. The theoretical description of the process involves the exchange of a pomeron between the proton and the photon (figure 1a). In figure 1a the photon virtuality is labelled $-Q^2$, the mass of the vector meson $m_V$ and the four momentum transfer squared at the proton vertex $t$. In the absence of a hard scale ($Q^2, t, m_V < 2$ GeV$^2$) the soft pomeron of Regge theory may be used to give an adequate description of the data. If either $Q^2$, $t$ or $m_V$ is large ($> 2$ GeV$^2$) the data [1, 3, 4, 5] are no longer consistent with the expectations of Regge theory. Rather they indicate that models of the pomeron based on perturbative QCD may be applicable. One feature of the QCD calculation is that the cross section for the photoproduction of vector mesons is expected to depend on the gluon density squared. This means that the elastic vector meson photoproduction cross section is particularly sensitive to the gluon density. The masses of the $\Upsilon$, $\psi'$ and $J/\psi$ are large enough that the QCD calculations of elastic photoproduction cross sections are expected to be valid.

This paper is organised as follows. Section 2 describes the trigger system and the DST selection used to acquire the data, the final event selection criteria are described in section 4, the muon chamber efficiency and the Monte Carlo generators used to study the signal and the background are described in section 3 and 6, respectively. The kinematics and acceptance for the process $ep \to epV$ is described in section 7. This is followed by a discussion of the contributions to the signal (section 8) and of the systematic errors in the cross sections (section 9). The photoproduction cross section is presented as a function of the $\gamma p$ centre of mass energy ($W$) in section 10. Finally, conclusions are drawn in section 11.

## 2 Trigger and DST selection

**Important Remark**

This analysis is in many respects the continuation, on a much larger data sample, of the recently published paper [2] based on the 94 luminosity. All the knowledge gained for this paper was fed into a particular fast selection DST bit (b101).

Events are flagged by this bit if they satisfy the following requirements:

- they have triggered at least one of the muon FLT trigger slots 8,9,10,11,14,15;
- they have triggered at least one of the muon SLT trigger slots MU01, MU02;
- they have triggered the TLT GLOMU slot;
- they have two and only two tracks (that is 2 tracks both in the VCTRHL and in the VCTPAR tables);
- the two tracks have opposite charges;



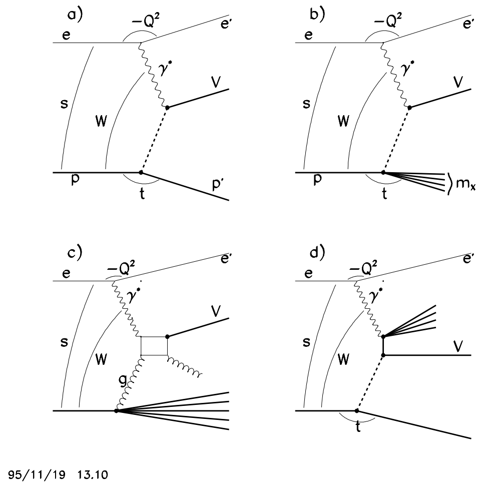


Figure 1: Generic Feynman diagrams for the electroproduction of a vector meson. The mechanism for elastic vector meson production via 'pomeron-photon fusion' is shown in (a). The pomeron is represented by the dashed line. The electron proton centre of mass energy squared is labelled $s$, the photon proton centre of mass energy is labelled $W_{\gamma p}$, the vector meson, $V$, has mass $m_V$, $-Q^2$ is the four momentum transferred at the electron vertex and $t$ is the four momentum transferred at the proton-pomeron vertex. Proton dissociative photoproduction is shown in (b). The proton dissociates into a hadronic system of invariant mass $m_X$ (c) Illustrates the mechanism for inclusive inelastic vector meson photoproduction via the colour singlet model [7]. (d) Illustrates the mechanism for photon dissociation in vector meson photoproduction.



- the distance of minimum approach to the beamline in the $xy$ plane of both tracks is less than 2 cm (for cosmic ray rejection);
- the cosine of the angle between the two tracks at the interaction point ($\cos\Omega$) has to be greater than -0.995 (for cosmic ray rejection);
- the invariant mass is greater than 2 GeV.

For this analysis only the data flagged by this bit and that fired one of the FLT trigger slots: 8, 10 and 11 are considered. Events from the slots 9, 14 and 15 were used for checks only.

In the following paragraph we describe the trigger slots and compare important physical quantities for the data and the MC simulation.

**First Level Trigger**

Slot 8 imposes the following requirements:

- Hits in the inner barrel muon chambers (BMUI) in coincidence with an energy deposit of at least 0.464 GeV summed over the full calorimeter.

or

- Hits in the RMUI chambers in coincidence with an energy deposit of at least 0.464 GeV in RCAL.
- No more than five tracks in the CTD.
- The tracks satisfy the logic $flag1.OR.flag2.OR.flag3$, $flagi$ ($i = 0, 1, 2, 3$) are the classification bits for the tracks.
- The energy in the FCAL cells surrounding the beam pipe less than 3.75 GeV. This cut was designed to eliminate events in which the proton remnants were detected in the main calorimeter.

Slots 10 and 11 impose the following requirements:

- Coincidence between barrel (slot 10) or rear (slot 11) muon inner chambers and at least one of the corresponding 12 isomu regions of the calorimeter.
- CTD tracks that satisfy the $flag1.OR.flag2.OR.flag3$ logic.

For all three trigger slots, Veto signals must not come from the Veto Wall, the SRTD and the C5 detectors. Furthermore, the CTD rejects events with $noTRKvld$ and $TRKVeto$ signals activated.

These three slots had prescale equal 1 all over the years.

Trigger slot 9 requires the presence of signals in the inner muon chambers in coincidence with a signal above a threshold of 4978 MeV in the LUMI electron calorimeter. There is no use of the calorimeter. This slot was heavely prescaled during 1997. Trigger slots 14 and 15 require the presence of a signal both in the inner and outer muon chambers with a minimum energy deposit in the whole calorimeter of at least 0.464 GeV if a coincidence signal is detected in the inner and outer barrel muon chambers, 0.464 GeV in RCAL if a coincidence signal is detected in in the inner and outer rear muon chambers. Slots 9, 14 and 15 have the same tracking requirements of Slots 8, 10 and 11.

Figures from 2 to 7 show some comparisons between data and DIPSI MC simulation. In all plots the data are represented by crosses while the MC simulation is shown as a histogram.

Figure 2 shows the fired FLT muon chamber sectors.

Figure 3 shows the FLT tower energy. Figure 4 shows the fired FLT ISOMU sectors.

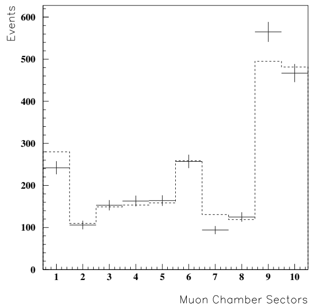


Figure 2: The distribution of the fired inner muon chamber sectors at FLT level. The crosses are the data, the histogram is the MC calculation.



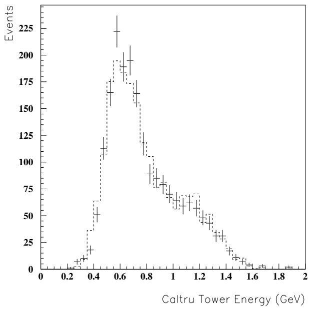


Figure 3: The energy distribution released by a muon in the calorimeter trigger. Data are shown as crosses while the result of the same calculation performed on the DIPSI Monte Carlo is shown as the histogram. The data and the Monte Carlo agree well over the full range of trigger tower energies.



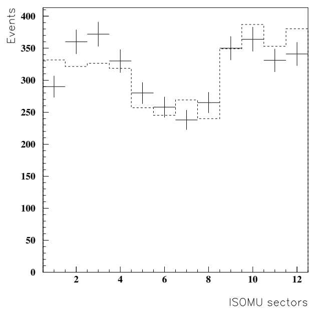


Figure 4: The distribution of the fired ISOMU sectors. The crosses are the data, the histogram is the mC simulation.



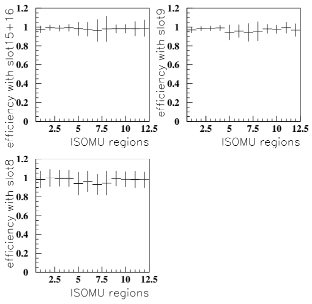


Figure 5: ISOMU regions efficiency obtain with slot 15+16, slot 9 and with slot 8 respectively. The errors are statistical.

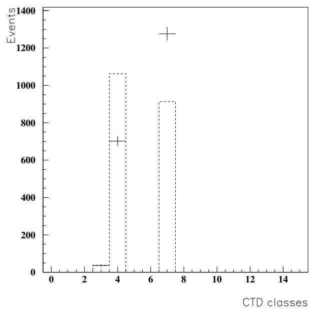


Figure 6: The observed CTD classes distribution. The crosses are the data, the histogram is the MC simulation.

In fig. 5 we see the efficiency of the 12 ISOMU regions as obtained using the slot 8, slot9 and slot 14+15 respectively.
The figures 6 and 7 show the classification of the registered tracks in the accepted CTD classes and the CTD multiplicity. The agreement between data and MC looks satisfactory with the exception of the distributions in 6 and 7. The problem has been submitted to CTD experts.

**Second Level Trigger:**

- The Second Level Trigger (SLT) requires that the signals in FCAL and RCAL be in time with the beam crossing (beam gas rejection), and that the signals in BCAL be in time with the beam crossing (cosmic rejection).
- At the SLT the total energy in the calorimeter is calculated for all cells above threshold ($\Sigma E$) and also the $z$ component of the energy ($\Sigma p_Z = \Sigma_i E_i \cos\theta_i$). The ratio $\frac{\Sigma p_Z}{\Sigma E}$ is then required to be less than 0.96.
- The data have to be flagged by the FLT muon triggers.

**Third Level Trigger**

To trigger on low momentum muons coming from the interaction region a special third level filter named *GLOMU* was used. The algorithm is based on a search for a CTD track which would match with a signal consistent with the passage of a minimum ionising particle (m.i.p.) through the calorimeter and a track segment in the muon chambers. In detail, the algorithm proceeded as follows.



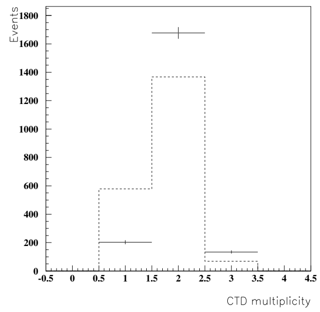


Figure 7: The track multiplicity observed in the CTD at FLT level. The crosses are the data, the histogram is the MC simulation.



1. Track segments were reconstructed in the barrel and rear muon chambers. The best track segment per chamber is selected and the position and direction of the track as it enters the chamber is recorded.
2. An attempt is made to match the muon chamber track segments with tracks measured in the CTD. To be considered a CTD track must satisfy the following criteria:
   - The CTD track fit $\chi^2$ should not exceed 20 (spurious track rejection).
   - The distance of closest approach of the track to the beam line should be less than 10 cm (cosmic rejection).
   - The $|z|$ coordinate of the track at its distance of closest approach to the beam line should not exceed 75 cm (beam gas rejection).
   - The polar angle of the tracks should exceed $20^0$. The trigger was designed to find muons entering the barrel and rear muon chambers (combinatorial reduction).
   - The track momentum must exceed 1 GeV for tracks in the rear direction. For tracks in the barrel region the transverse momentum was required to exceed 1 GeV. Tracks in the rear direction are defined as those which strike the flat circular rear end of the cylindrical reference surface defined below, barrel tracks strike the circular 'tube' section of the reference cylinder.

   A track satisfying these criteria is extrapolated from the point of closest approach to a fiducial surface (external to the CTD) using a Runge-Kutta technique taking into account the full magnetic field and the material traversed. The fiducial surface is a cylinder of radius 94 cm between $z = -146$ and $z = 180\ cm$. This surface was chosen as the magnetic field has dropped below 1 kGauss for all points on this surface. For each extrapolated track the position, direction and momentum is recorded.
3. A search is now made for clusters of energy in the calorimeter consistent with the passage of a m.i.p. Such a cluster was required to have an electromagnetic energy in the range 0 to 3 GeV, a hadronic energy in the range 0.5 to 8 GeV, to contain at least 1 and no more than 6 EMC cells and to contain at least one 1 and no more than 8 HAC cells. At this point the cluster timing is used to increase the cosmic rejection.
4. The matching $\chi^2$ is calculated for events in which a muon track segment, a m.i.p. cluster and a CTD track satisfying the above criteria are found. The matching $\chi^2$ is calculated separately in the azimuthal angle $\phi$ and polar angle $\theta$ as follows. Five determinations of these two angles are available:
   - $\theta, \phi$ from the CTD track.
   - $\theta, \phi$ from the B/RMUI track.
   - $\theta, \phi$ given by the segment connecting the CTD–CAL points.
   - $\theta, \phi$ given by the segment connecting the B/RMUI–CAL points.
   - $\theta, \phi$ given by the segment connecting the CTD–B/RMUI points. (This last constraint was not used in the trigger.)

   The $\chi^2$ sum of $\chi^2_\theta$ and $\chi^2_\phi$ is computed for all the combinations. From studies on Monte Carlo a loose cut at 20 on $\chi^2$ was used in order to accept events.

The performance of the TLT is investigated in figures 8 to 11. A comparison is made between the distributions of the triggering muon in $\cos\theta$ (figure 8), $\phi$ (figure 9), momentum (figure 10) and matching $\chi^2$ (figure 11) between the data and the Monte Carlo. In each case a good description of the data is obtained.

**Summary**



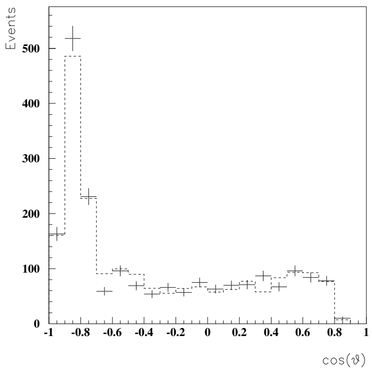


Figure 8: The distribution of $\cos\theta$ for the TLT track matched to the triggering muon. The data (solid points) are compared with the DIPSI Monte Carlo (dashed line).

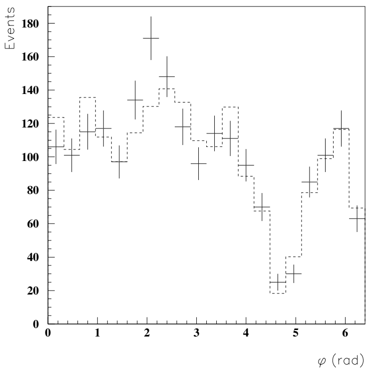


Figure 9: The distribution of $\phi$ for the TLT track matched to the triggering muon. The data (solid points) are compared with the DIPSI Monte Carlo (dashed line).



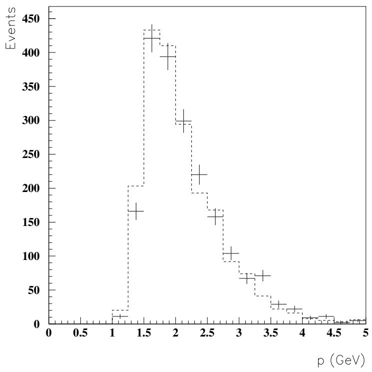


Figure 10: The distribution of momentum for the TLT track matched to the triggering muon. The data (solid points) are compared with the DIPSI Monte Carlo (dashed line).



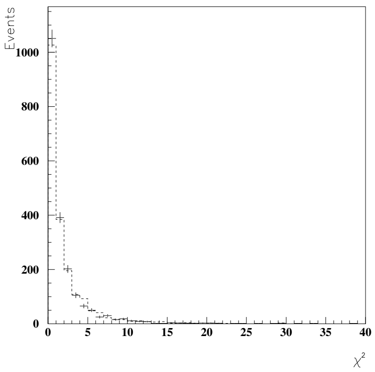


Figure 11: The distribution of matching $\chi^2$ for the triggering muon. The data (solid points) are compared with the DIPSI Monte Carlo (dashed line).



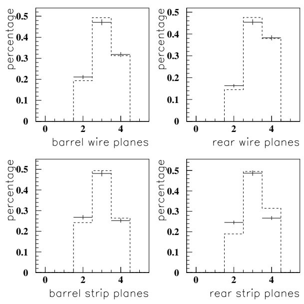


Figure 12: The percentage of fired planes for accepted tracks for the barrel and rear muon chambers. The crosses are the data, the histogram is the MC simulation.

The overall stability of the trigger is investigated in figure 13, the data are split into the three years of data taking, each bin corresponds roughly to 200 $nb^{-1}$. It can be seen that the number of events per luminosity was stable over the data taking period. In figure 14 it is shown the invariant mass plot at the output of the DST level summed over all the entire luminosity. The peaks of the $J/\psi$ and $\psi'$ are rather clear.

## 3 Muon Chamber Efficiency

A detailed study was done to understand and to simulate correctly the efficiency of the muon chambers. Especially time was spent to spot dead limited streamer tubes (LST). In fig. 12 we show, divided into barrel and rear regions, the percentage of fired planes for accepted tracks along the two views: wire-view, strip-view. We remember that each chamber has four planes and to build a track at least two planes for each views are necessary. A general good agreement is seen except for the rear strip plot, where a slight higher efficiency is visible in the MC simulation.

## 4 Final Event Selection

A sample of 22592 evtake events resulted from the procedure described in the previous sections. The following selection was applied to this sample as well as to the MC samples described in

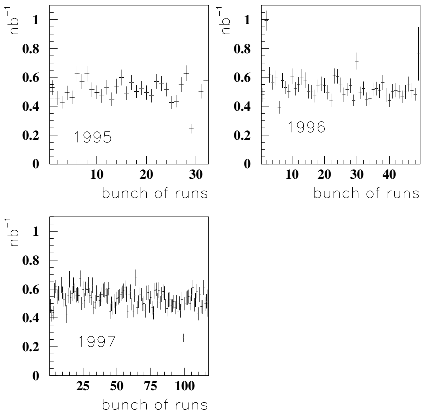


Figure 13: Overall stability of the trigger: the data are split into the three years of datataking, each bin corresponds roughly to 200 nb$^{-1}$. The trigger rate is constant over the running period.



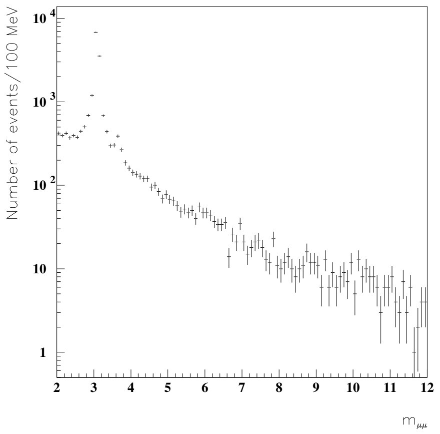


Figure 14: Invariant mass plot at the output of the dst level, the data correspond to all the available statistics.



section 6 used for the analysis.

- Colinearity was recomputed with the more precise track parameters of the vctpar table and the cut $\cos(\theta) > -0.995$ applied.
- At least one segment had to be reconstructed in the muon chambers with the more stringent offline algorithm.
- A fit between a CTD and B/RMU tracks was sought by the following procedure: each track in the VCPARCAL table is extrapolated by the VCVXTRP Phantom routine to a plane normal to it and passing by the MBXYSG segment center; VCVXTRP conveniently extrapolates to a plane that is essentially the chamber plane, so the errors on the extrapolated coordinates in the plane are independently measured by B/RMU and can be added in quadrature to the coulomb displacements.The r.m.s Coulomb displacement is computed by big steps to to EMC, HAC1 (HAC2), muon chamber. The number of radiation lenghts is taken from the blue book; at each step the mip average energy loss as found by MC (LPAIR) is applied to the track energy; a $\chi^2$ is defined as the sum of the squares of the ratios of the displacements found on the two extrapolated coordinates an the respective errors. Figure 15a,b, show the $\chi^2$ distributions for barrel and rear respectively.

  A slope of -0.5 and an average of 2 is expected for a chi2 distribution with 2 degrees of freedom. The agreement is good in the barrel, showing a satisfactory understanding of the media between CTD and BMU, a little less so for the rear; the very irregular configuration of the field in that region may be at least partially responsible for it.
- The mass is recomputed with the VCTPAR parameters and the cut at 2 GeVapplied.

  Figure 19a compares the mass spectra of data and of the LPAIR Bethe-Heitler simulation normalized to lumi at this level of selection.
- At least superlayers 1,3 are required on both tracks.

  Figure 19b compares the mass spectra of data and of the LPAIR Bethe-Heitler simulation normalized to lumi at this level of selection.
- After applying the noise suppression routine noise96s, SINISTRA95 is called to identify electrons. The events for which an electron is found are excluded by any further analysis (in this paper).
- The package CALTRACK of the Phantom library is then used to associate calorimeter cells to tracks.

  Figure 16 plots the energy associated in the HAC section of CAL against that associated in the EMC section, for the CTD track tagged by the muon chambers (a) and for the untagged (second) track (b). Both figures display the pattern of a minimum ionizing particle, as was required at TLT for the tagged track, and no cut is imposed on this account.
- Figure 17a shows the CAL energy, not associated to tracks, in the forward $\eta$ cone for MC elastic events simulation (Bethe-Heitler) and the cut applied.

  Fig 17b shows the CAL energy, not associated to tracks, in the remaining part of the calorimeter. The presence of electrons non recognized by SINISTRA95 is manifest. A cut is applied at 2.5 GeVon this energy.



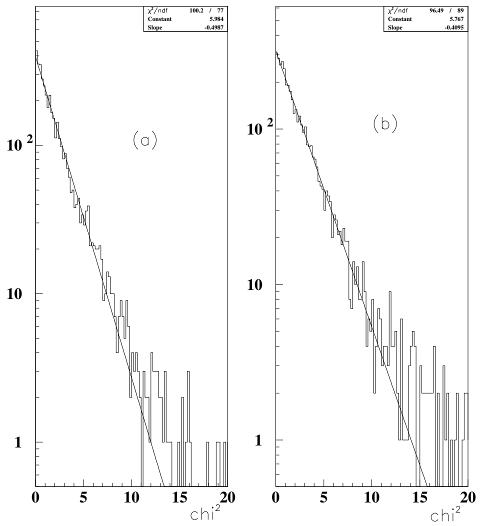


Figure 15: $\chi^2$ distribution of the offline CTD-B/RMU match for barrel (a) and rear (b) muon chambers.

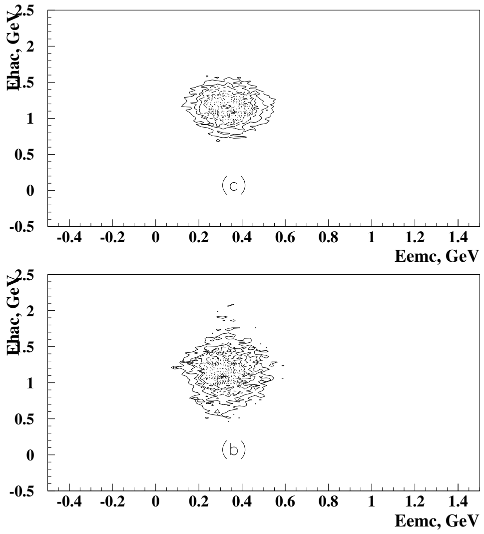


Figure 16: Energy associated in the HAC section of CAL against that associated in the EMC section to tagged muons (a) and to the untagged ones in the selected sample.



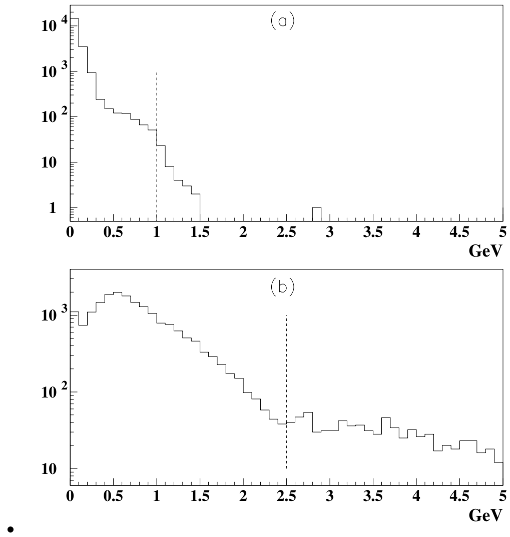


Figure 17: CAL energy, not associated to tracks, in the forward $\eta$ cone for MC elastic events simulation (Bethe-Heitler) and the cut applied.



| cut | A DATA remaining events | B DATA % | C DATA $J/\psi$ % | D DIPSI $J/\psi$ % | E EPSOFT % | F LPAIR elastic % | G LPAIR dissoc. % |
|---|---|---|---|---|---|---|---|
| (a) evtake b101 | 22592 | 100 | - | 100 | 100 | 100 | 100 |
| (b) colinearity(vctpar) | 22512 | 99.6 | - | 100 | 100 | 99.8 | 100 |
| (c) track in B/RMU | 22341 | 98.9 | - | 100 | 100 | 99.8 | 100 |
| (d) CTD-B/RMU match | 21698 | 96.0 | - | 99.4 | 99.3 | 99.2 | 99.4 |
| (e) mass > 2 GeV | 21687 | 96.0 | 100 | 99.4 | 99.3 | 99.1 | 99.2 |
| (f) SL 1-3 (both tracks) | 17974 | 79.6 | 95 | 88.7 | 89.2 | 84.8 | 85.2 |
| (g) $Q^2 = 0$ | 16543 | 73.2 | 88.5 | 83.9 | 87.9 | 77.1 | 77.4 |
| (h) CALE($\eta > 1.5$) < 1 GeV | 11927 | 52.8 | 66.0 | 83.9 | 46.8 | 77.0 | 48.6 |
| (i) CALE < 3.5 GeV | 11139 | 49.3 | 62.4 | 79.7 | 45.8 | 72.9 | 46.3 |

Table 1: Comparison of the effects of the analysis cuts on the complete data sample, on the $J/\psi$ data sample and on the MC samples used in the analysis. Cuts on CAL energy not associated to the muons (CALE) keep 86-89 % of the elastic events ((i)/(f) of columns D and F) against 52-54 % of the p-dissociative ones (columns E,G).

Table 1 summarizes the effect of the cuts on the data and on the MC simulation used in the analysis.
Figure 19c compares the mass spectra of data and of the LPAIR Bethe-Heitler simulation normalized to lumi at this level of selection. The progressive disagreement of the data and the LPAIR Bethe-Heitler simulation is evident. Bethe-Heitler is a QED process. Its elastic part in particular is well calculable. Some light on this problem is shed by Figure 18 where the $\theta$ distribution of data is compaired with that of LPAIR, normalized to Lumi.

## 5 Events Numbers

The numbers of $J/\psi$ and $\psi'$ events is evaluated as follows:

- Figure 20 shows the data in the mass region 2 to 5 GeVwith superimposed the normalized Bethe-Heitler background.
- Figure 21 shows the data after subtraction of the Bethe-Heitler background and superimposed the mass distribution of $J/\psi$ simulated by DIPSI and normalized to the number



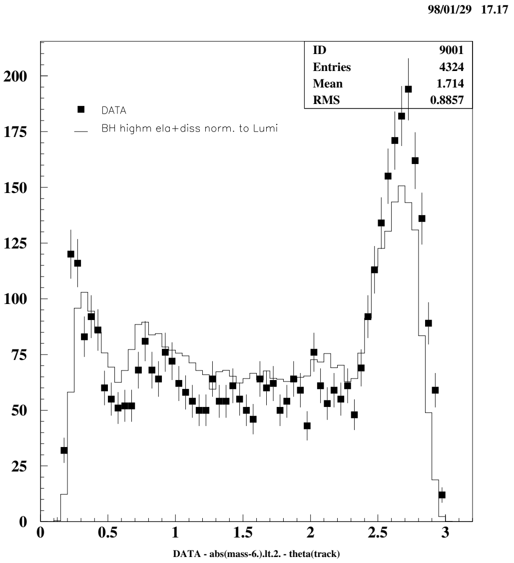


Figure 18: Comparison of the data track distribution in $\theta$ with predicted by the LPAIR MC, normalized to Lumi.

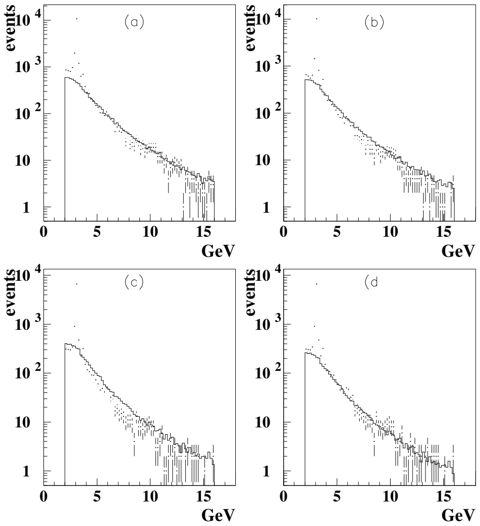


Figure 19: Comparison of data with LPAIR normalized to lumi at various selection levels. (a) corresponds to level (e) of table 1, (b) to level (f) and (c) to the final level (i). (d) compares data with LPAIR normalized to 0.65 Lumi. The disagreement is clear borh in normalization and in shape.



| P1 | P2 | P3 | P4 | P5 | P6 | P7 |
|---|---|---|---|---|---|---|
| $7.568 \pm .074$ | $-0.682 \pm .020$ | $1.9 \pm 3.2$ | $-0.16 \pm 0.26$ | $5.247 \pm 1.637$ | $9.829 \pm 0.168$ | $0.484 \pm .214$ |

Table 2: Parameters to the mass distribution of Figure 24d. The $\chi^2$ of the fit is 34/53 dof.

of events within $\pm 0.1$GeV from the central value. MC is seen to reproduce the shape of the distribution well. The total number of $J/\psi$ is therefore taken from it.

- Figure 22 shows the mass distribution of the data after subtraction of the DIPSI $J/\psi$ of Fig. 21 and superimposed on it the DIPSI simulation of the $\psi'$ normalized to the three central bins of the signal.
- Figure 23 finally shows the complete data distribution compared with the sum of the Montecarlo contributions described above.

$\Upsilon$counting

- Figure 24a shows the data mass distribution *perse* while figure 24b shows again that the simulated Bethe-Heitler process, even renormalized to the data, does not reproduce the data well. The prejudice was then applied that background should be smooth outside the resonance region. Figure 24c shows that a double exponential to the mass region above the $J/\psi$ and $\psi'$ and outside the $\Upsilon$region fits the data well. A global 2 exponential plus a gaussian fit was then performed and is shown in Figure 24d. The $\chi^2$ of the fit is 34/53 dof. The fit parameters are reported in the table 2. A gaussian fit to the $\Upsilon(1S)$, $\Upsilon(2S)$ and $\Upsilon(3S)$ found in the literature $(1 : 0.32 : 0.13)$ yields a mean of 10.04 and a width of 0.56 GeV, compatible with P6 and P7 in the table. From P5 and P7, given the binning of 0.2 GeV, one computes a signal of $32 \pm 10$ events. A second analyisis [24] finds $26.1 \pm 11.2$ events.

# 6 Monte Carlo

- The reaction $e^+p \to e^+ \ V \ p$, $V = \Upsilon \ ,\psi', \ J/\psi$ (figure 1a) was modelled using the DIPSI Monte Carlo program [13]. DIPSI is based on a model of vector meson production in which the positron radiates a photon which fluctuates into a virtual quark anti-quark ($q\bar{q}$) pair [6]. The momentum required to produce an on shell meson is supplied via the exchange of a pomeron between the $q\bar{q}$ pair and the proton. The pomeron is described as a gluon ladder evaluated in the leading logarithm approximation of QCD. In this model the cross section is proportional to $[\alpha_s \bar{x} g(\bar{x}, \bar{q}^2)]^2$ where $\alpha_s$ is the strong coupling constant (assumed constant) and $\bar{x} g(\bar{x}, \bar{q}^2)$ is the gluon momentum density in the proton. The quantities $\bar{x}$ and $\bar{q}^2$ are given by

$$\bar{x} = \frac{Q^2 + m_{J/\psi} - t}{W^2} \qquad \bar{Q}^2 = \frac{Q^2 + m_{J/\psi} - t}{4} \tag{1}$$

and give the effective momentum fraction and scale at which the gluon density is probed respectively. For elastic $J/\psi$ photoproduction $\bar{q}^2$ takes a value of approximately 2.5 GeV$^2$



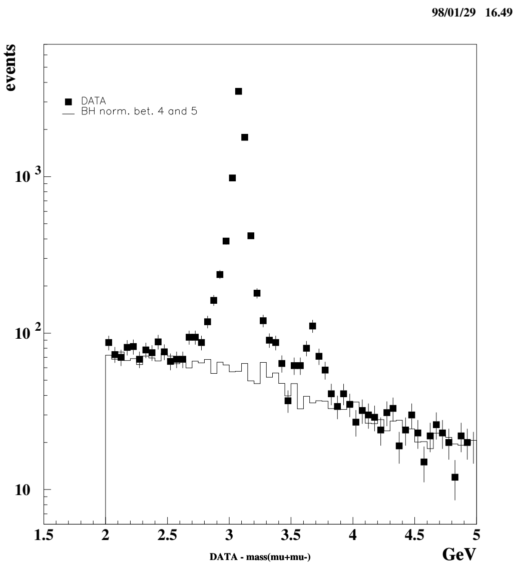


Figure 20: Data mass distribution with the Bethe-Heitler background estimated by normalizing the BH distribution to the 4 to 5 mass region.



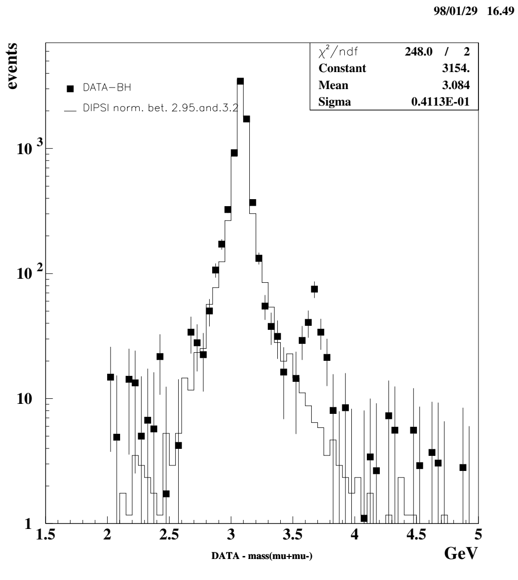


Figure 21: Data mass distribution after subtraction of the Bethe-Heitler background with the $J/\psi$ contribution obtained by normalizing the MC simulation to the events within $\pm 0.1$GeV from the signal mean.

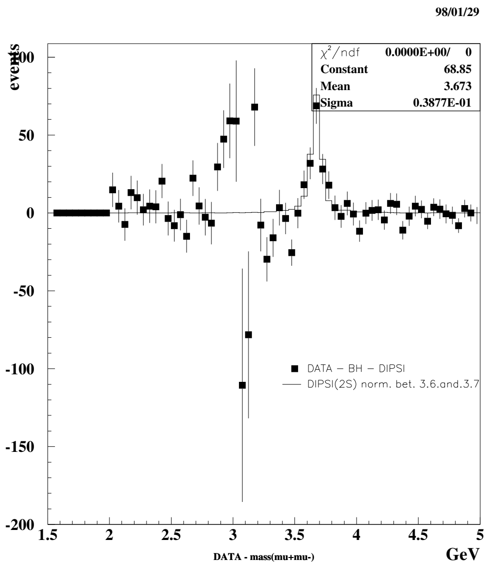


Figure 22: Data mass distribution remaining after subtraction of the Bethe-Heitler and the $J/\psi$ with the normalized DIPSI $\psi'$ simulation.



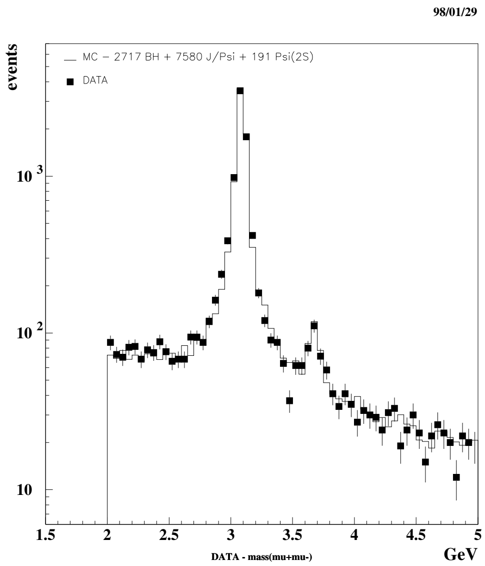


Figure 23: Data mass distribution compared with the sum of the MC estimated contributions of Bethe-Heitler, $J/\psi$, $\psi'$.



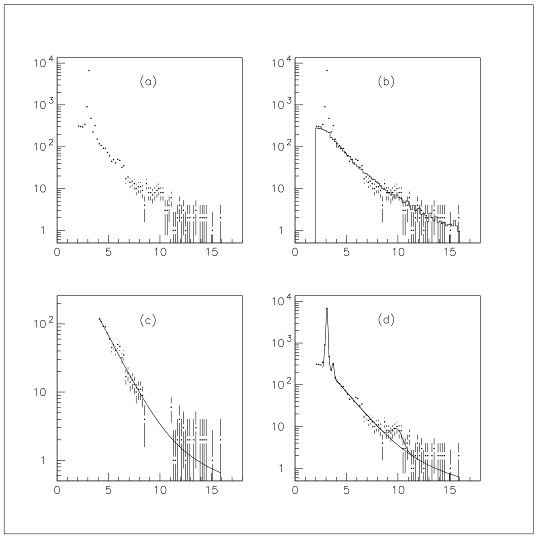


Figure 24: (a)data mass distribution, (b) same with LPAIR simulation normalized to events between 4 and 8 GeV, (c) two exponential fit to mass region outside resonances, (d) two exponential plus gaussian fit.



[6] while the process is sensitive to $\bar{x}$ in the range $0.4 \times 10^{-3} < \bar{x} < 6 \times 10^{-3}$, for $\psi'$ ..., for $\Upsilon$...

Events were generated in the $W$ range $20 < W < 210$ GeV and between the smallest value of $Q^2$ kinematically allowed ($Q^2 \approx 10^{-9}$ GeV$^2$) and $Q^2 = 4$ GeV$^2$. The events were then passed through a detailed simulation of the ZEUS detector and trigger. The simulated events were then subjected to the same reconstruction and analysis programs as the data.

Samples of 60000 , 20000 and 20000 generated events respectively have been used in this anlysis for $J/\psi$, $\psi'$ and $\Upsilon$.

- The EPSOFT Monte Carlo [14] have been used to simulate diffractive $J/\psi$ production, $\gamma^* p \to J/\psi X$, in which the incoming proton undergoes diffractive dissociation into an hadronic system $X$. EPSOFT is based on the assumption that the diffractive cross section is of the form $d\sigma/d|t|dM_N^2 \propto e^{-b|t|}/M_N^\beta$ where $M_N$ is the mass of the dissociative system. The simulation of the hadronisation of the dissociative system includes a parameterisation of the resonance spectrum.

  A sample of 20000 generated events were used for this analysis.

- The Monte Carlo LPAIR was designed to simulate lepton pair production (such as $e^+e^-$, $\mu^+\mu^-$ and $\tau^+\tau^-$) via the two-photon process in the $e^+e^-$, $p\overline{p}$ and $e^-p$ interactions. It is based on Vermaseren's generator [10] and was developed with improvements, especially to the treatment of inelastic modes. The generator was first interfaced to the H1 software [11]. The interface for ZEUS [12] has been written according to the scheme defined in ZDIS. There are two mechanisms by which lepton pairs may be produced in the two-photon processes:

  - The elastic process in which a proton interacts elastically,
    i.e. $e^- + p \to e^- + \mu^+ \mu^- + p$.
  - The inelastic process in which a proton interacts inelastically and undergoes diffractive dissociation,
    i.e. $e^- + p \to e^- + \mu^+ \mu^- + X$.

  The two exchanged photons in the t-channel interact and produce a pair of leptons. The generator has been applied for the study of background contamination to elastic $J/\psi$, $\psi'$and $\Upsilon$ production. Theoretical cross sections corresponding to elastic and inelastic processes are $1.413 \pm 0.003$nb and $0.484 \pm 0.002$nb for muon pairs production. Also the elastic $\tau^+ \tau^-$ production with subsequent semileptonic decay into muons wa studied. The theoretical cross sections is 106 pb and no contamination is predicted.

Samples of 1.2x $10^6$ elastic and 2x $10^5$ proton dissociative events, corresponding to 842.70 $pb^-1$ and 409.0 $pb^-1$ equivalent luminosity respectively, were generated for this analysis but processed through the selection simulation chain only if the generated mass was $>$ 4 GeV, in an effort to understand the high mass background.
Smaller independent samples of $10^5$ elastic ( equivalent luminosity 70.15 $pb^-1$) and 2 $10^4$ (equivalent luminosity 40.54$pb^-1$) proton dissociative events were processed for any generated mass value.
Figure 25 shows that no distortion has been introduced in the reconstructed mass distribution above 4.2 GeVby the cut in the generated mass.

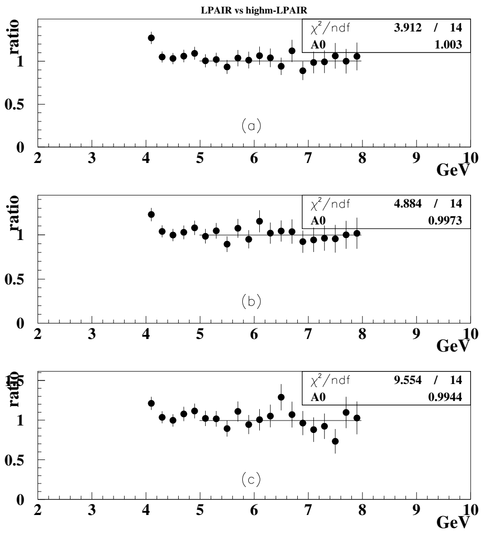


Figure 25: Ratio of generated mass cut and uncut elastic LPAIR samples, normalized to lumi, at various selection levels.



# 7 Kinematics and Acceptance

Diffractive vector meson $V$ photoproduction (figures 1a b and d) is characterised by final states in which the $V$ is accompanied by a hadronic system of mass $m_X$ resulting from the diffractive dissociation of the proton or of the photon. In the case of proton dissociation the dominant contribution to the cross section occurs when $m_X \sim m_p$ (where $m_p$ is the proton mass) - ie the hadronic system $X$ has very low transverse momentum. Experimentally this has the consequence that elastic (figure 1a) and proton dissociative (figure 1b) $V$ production are indistinguishable in the ZEUS detector. The section below describes the kinematics of elastic photoproduction (figure 1a) and investigates the acceptance of the ZEUS detector to this process.

Let the incoming (outgoing) proton four momentum be denoted by $P$ ($P'$), $j$ be the four momentum of the $V$, the incoming and outgoing positron four momenta be $k$ and $k'$ respectively, and the four momentum of the two leptons from the $V$ decay be $l_1$ and $l_2$. Then, the four momentum transfer is given by $q = k - k'$ and $Q^2 = -q^2$ is given by

$$Q^2 = -q^2 = -(k - k')^2 \tag{2}$$

The $e^+p$ centre of mass energy squared $s$ is given by

$$s = (P + k)^2 \tag{3}$$

The Bjorken scaling variable $y$ is given by

$$y = \frac{P.q}{P.k} \tag{4}$$

while the Bjorken $x$ scaling variable is given by

$$x = \frac{Q^2}{2P.q} = \frac{Q^2}{sy} \tag{5}$$

The four momentum of the $V$ is given by

$$j = l_1 + l_2 = (E_j, \mathbf{p_{T(j)}}, j_z) \tag{6}$$

The elasticity $z$ is defined by the equation

$$z = \frac{P.j}{P.q} \tag{7}$$

$z$ lies between 0 and 1. Elastic $V$ photoproduction is characterised by $z = 1$, in inelastic $V$ photoproduction $z$ is less than 1.

If the photon is emitted collinear with the beam axis and $z = 1$ then

$$t = (P - P')^2 = (q - j)^2 = -Q^2 - p^2_{T(j)} \tag{8}$$

where $p^2_{T(j)}$ is the momentum of the $V$ transverse to the beam axis. Assuming $Q^2 \approx 0$

$$t \approx -P^2_{T(V)} \tag{9}$$

At HERA

$$P = (E_P, 0, 0, E_P) \tag{10}$$



and the four momentum of the photon may be written

$$q = (q_0, q_x, q_y, q_z) \tag{11}$$

So that

$$z = \frac{E_j - j_z}{q_0 - q_z} \tag{12}$$

The sum of the Mandelstam $s, t$ and $u$ variables is equal to the sum of the masses in two body scattering, so that

$$W^2 + t + u = -Q^2 + 2m_p^2 + m_j^2 = (-Q^2 + m_p^2 + 2P.q) + t + (m_p^2 + m_j^2 - 2P.j) \tag{13}$$

where $m_j$ is the $V$ mass. This may be rearranged to give

$$0 = 2E_p[(q_0 - q_z) - (E_j - j_z)] \rightarrow 0 = 2E_p[1 - z] \tag{14}$$

so that for elastic $V$ photoproduction $z = 1$.

The photon-proton centre of mass energy $W$ is given by

$$W^2 = (P + q)^2 = sy - Q^2 \tag{15}$$

In the approximation $Q^2 \approx 0$

$$W^2 = sy \tag{16}$$

The $ep$ cross section rises rapidly as $Q^2$ tends to zero so the scattered positron is rarely seen in the main detector. As a result the kinematic variables must be reconstructed from the decay leptons of the $V$. The scaling variable $y$ is determined using the Jacquet Blondel method [8]

$$y_{JB} = \frac{E_j - j_z}{2E_k} \tag{17}$$

where $E_k$ is the positron beam energy. $W$ is then given by

$$W^2 = 2E_p(E_j - j_z) \tag{18}$$

The DIPSI Monte Carlo (see section 6) has been used to study the reconstruction of the kinematic variables. The events were generated as described in section 6. The response of the detector to these events was then simulated using the NumXXX version of Mozart and the simulated events reconstructed using the same programmes as for the real data. The reconstructed events had to pass the full event selection.

In figure 26a the solid line shows the generated $Q^2$ distribution while the shaded histogram shows the $Q^2$ of the accepted events. The ratio of the true accepted and generated $Q^2$ distributions is plotted in figure 26b. The ratio is flat over the range $Q^2 < 1$ GeV$^2$ but falls rapidly for values of $Q^2$ greater than 1 GeV$^2$.

The reconstruction of $y$ is investigated in figure 27. In figure 27a the solid line shows the generated $y$ distribution while the shaded histogram shows the true $y$ of the accepted events. The ratio of the true accepted and generated $y$ distributions is plotted in figure 27c. The value of $j_{JB}$ at which the $J/\psi$ is produced at rest is indicated. The acceptance is high at this point. Figure 27b shows the reconstructed $y$ (using the Jacquet Blondel method) as a function of the generated $y$. It is evident that $y$ is well measured over the whole of the kinematic range.



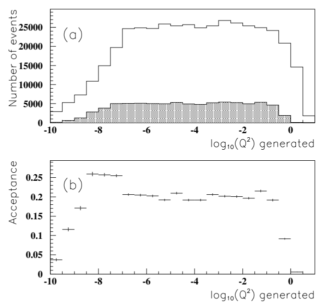


Figure 26: The generated $Q^2$ distribution is shown in (a) as the solid line, while the accepted distribution is shown as the shaded histogram. The ratio of the accepted and generated $Q^2$ distributions is plotted in (b).

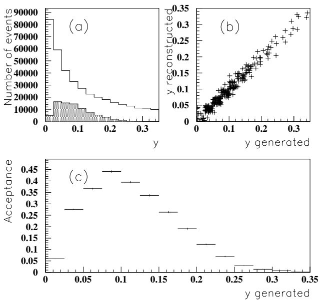


Figure 27: Investigation of the reconstruction of $y$. The generated $y$ distribution is shown in (a) as the solid line, while the accepted distribution is shown as the shaded histogram. The correlation between the reconstructed and generated $y$ is shown in (b). The ratio of the true accepted and generated $y$ distributions is plotted in (c).



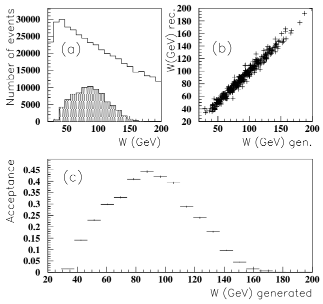


Figure 28: Investigation of the reconstruction of $W$. The generated $W$ distribution is shown in (a) as the solid line, while the accepted distribution is shown as the shaded histogram. The correlation between the reconstructed and generated $W$ is shown in (b). The ratio of the true accepted and generated $W$ distributions is plotted in (c).

The reconstruction of $W$ is investigated in figure 28. In figure 28a the solid line shows the generated $W$ distribution while the shaded histogram shows the true $W$ of the accepted events. The ratio of the true accepted and generated $W$ distributions is plotted in figure 28c. Since $W$ is directly related to $y_{JB}$ via equation 16 the limits on $y_{JB}$ imply that $W$ must lie in the range $30 < W < 170$ GeV. Figure 28b shows the reconstructed $W$ as a function of the generated $W$. It is evident that $W$ is well measured over the whole of the kinematic range accepted ($40 < W < 160$ GeV).
The reconstruction of $p_{T(j)}$ is investigated in figure 29. In figure 29a the solid line shows the generated $p^2_{T(j)}$ distribution while the shaded histogram shows the true $p^2_{T(j)}$ of the accepted events. Figure 29b shows the reconstructed $p^2_{T(j)}$ as a function of the generated $p^2_{T(j)}$. It is evident that $p^2_{T(j)}$ is well measured over the whole of the kinematic range. The ratio of the true accepted and generated $p^2_{T(j)}$ distributions is plotted in figure 29c.

# 8 Backgrounds

## 8.1 Contributions to the Background

In the present analysis we wish to determine the cross section for elastic $J/\psi$, $\psi'$, $\Upsilon$ photoproduction (figure 1a). The event selection algorithms descibed in section 4 are designed to select



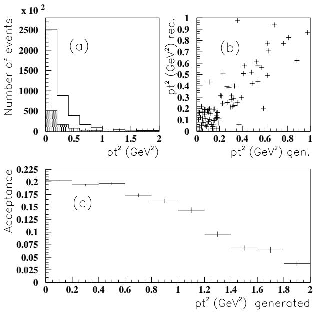


Figure 29: Investigation of the reconstruction of $p^2_{T(j)}$. The generated $p^2_{T(j)}$ distribution is shown in (a) as the solid line, while the accepted distribution is shown as the shaded histogram. The correlation between the reconstructed and generated $p^2_{T(j)}$ is shown in (b). The ratio of the true accepted and generated $p^2_{T(j)}$ distributions is plotted in (c).



events in which only the vector meson is observed in the main ZEUS detector. The following processes may contribute to the final sample in addition to elastic vector meson photoproduction:

- The Bethe-Heitler process in which a lepton pair is produced when a photon radiated by the positron fuses with a photon radiated by the proton. This process was simulated using the LPair Monte Carlo [9], [10], [11] modified for ZEUS as described in [12]. Two types of reaction must be distinguished:
  1. $ep \to ep\mu^+\mu^-$ ($l$ represents a lepton - either electron or muon). In this case the proton remains intact.
  2. $ep \to eX\mu^+\mu^-$. In this case the proton dissociates.

  This process gives the non-coherent background common to all the three resonances.

Then there are specific coherent contributions for each vector meson:

- Proton dissociative $J/\psi$ production (figure 1b). This is the dominant contribution to the background. The distribution of the mass ($m_X$) of the hadronic system resulting from the dissociation of the proton falls rapidly. Proton dissociative events with low $m_X$ leave no hadrons in the main ZEUS detector and so can not be distinuished from truely elastic events. The EPSOFT Monte Carlo was used to simulate this process.
- $\psi'$ production and decay. The $J/\psi$ is produced via the production and decay of $\psi'$. The only $\psi'$ decay mode giving a significant contribution to the $J/\psi$ signal is $\psi' \to J/\psi\ \pi^0\pi^0$ for which the branching ratio ($\mathcal{B}_C$) is $(18.4 \pm 2.7)\%$ [15]. The contribution is 3%, which is subtracted from the cross section.
- Proton dissociative $\Upsilon$ production. Due to the low statistics for the $\Upsilon$ and the lack of other informations we use for the $\Upsilon$ the same values obtained for the $J/\psi$.
- Contribution of the $\Upsilon(2S)$ and $\Upsilon(3S)$. They may contribute to the number of events in the $\Upsilon$ range either directly or via the chain

$$\Upsilon(2S) \to \Upsilon\ \pi^o\ \pi^0 \tag{19}$$

$$\Upsilon \to \mu^+\mu^- \tag{20}$$

  Resolution does not allow to separate the $\Upsilon$'s with present statistics. Following a suggestion by Strikman [20] and previous experimental findings [17] a systematic of -20 % is folded in the error for the $\Upsilon$ cross section. By taking into account the known branching ratios this limits to $-1\%$ the error contributed by the chain above.

## 8.2 The $\psi' \to J/\psi\ \pi^0\ \pi^0$ Contribution

The $\psi'$ contribution to $J/\psi$ was determined studying the sample of events in which the $\psi'$ decayed to a muon pair (branching ratio ($\mathcal{B}_1 = 0.77 \pm 0.17)\%$ [15]). This sample was obtained using the same cuts as those used to isolate the $J/\psi$ muon pair sample. The data sample used corresponded to the same luminosity ( 43.3 pb$^{-1}$). A signal of $N_1 = 190 \pm 17$ events was found at the $\psi'$ mass. The ratio of the $\psi'$ and $J/\psi$ acceptances, computed by DIPSI, was 1.16 between 40 and 160 GeV.

| | A | B | C | D | E | F |
|---|---|---|---|---|---|---|
| | PRT1 % | PRT2 % | PRT1+PRT2 % | PRT1 % | PRT2 % | PRT1+PRT2 % |
| DATA 95 | 15.27 ± 2.41 | 17.94 ± 2.62 | 25.57 ± 3.12 | 6.67 ± 4.71 | 16.67 ± 7.45 | 16.67 ± 7.45 |
| DATA 96 | 12.06 ± 0.87 | 14.13 ± 0.94 | 21.04 ± 1.15 | 9.48 ± 2.12 | 8.06 ± 1.95 | 13.27 ± 2.51 |
| DATA 97 | 13.25 ± 0.56 | 14.62 ± 0.59 | 23.36 ± 0.74 | 9.58 ± 1.27 | 8.24 ± 1.18 | 15.29 ± 1.60 |
| DIPSI | 0.00 ± 0.00 | 3.02 ± 0.15 | 3.02 ± 0.15 | - | - | - |
| EPSOFT | 56.40 ± 1.28 | 39.52 ± 1.07 | 74.30 ± 1.47 | - | - | - |
| LPAIR | - | - | - | 0.00 ± 0.00 | 0.23 ± 0.04 | 0.23 ± 0.04 |
| difLPAIR | - | - | - | 45.29 ± 1.15 | 41.29 ± 1.10 | 65.10 ± 1.38 |

Table 3: Percentage of events with hits in the PRT counters for the three data taking periods considered in this analysis and for the DIPSI ($J/\psi$), EPSOFT and LPAIR samples. MC simulation corresponds to the 96 data taking. The events in the samples are inside the cuts for the $J/\psi$ cross section calculation in columns A,B,C and inside a the control region 4 < mass < 8 GeV in columns D,E,F.

The number of events from $\psi'$ production entering the elastic $J/\psi$ sample via the decay $\psi' \to J/\psi\ \pi^0\ \pi^0$ was estimated using the formula

$$N_C = \frac{N_1}{\mathcal{A}_1\ \mathcal{B}_1}\mathcal{A}^{\mu}_C\mathcal{B}_C\mathcal{B} \tag{21}$$

where $\mathcal{B}$ is the branching ratio for the decay $J/\psi \to \mu^+\mu^-$, $\mathcal{B}_C$ is the branching ratio for the decay $\psi' \to J/\psi\ \pi^0\ \pi^0$.
The formula (21) leads to a $\psi'$ contamination of (3±)%.

### 8.3 The Contribution from Proton Diffractive Dissociation

The amount of p-diffractive events remaining in the sample is estimated by means of the PRT counters. Table 3 compares the fractions of events tagged by the PRT in two regions of the mass spectrum, namely at the $J/\psi$ and in the Bethe-Heitler dominated region 4 < mass < 8 GeV. By weighting the elastic and proton dissociative Bethe-Heitler by their known cross-sections and by the acceptance reported in table 1 one expects 14.9 % tagged events, in excellent agreement with the 14.7 ± 1.3 found for the '96 and '97 weighted average.



## 9 Systematic Errors

The following systematic effects that can bear on the $J/\psi$ and/or $\Upsilon$ cross sections have been considered:

- Background subtraction. This affects mostly the $\Upsilon$. As mentioned in 5 the parameters (center and width) obtained for the gaussian by the fit to the mass distribution are consistent with MC simulation. Letting the height of the gaussian vary within the estimated error leads to a variation of ± 10 in the $\Upsilon$'s count where the statistical error would be ±8 . Fitting a single exponent plus a gaussian in a restricted region around the signal leads to a count of 21 events in the signal. We take ±10 as global error for the $\Upsilon$'s count.
- Contribution of the $\Upsilon(2S)$ and $\Upsilon(3S)$. The contribution quoted in 8 are used as a systematic error (negative only).
- The systematics coming from the trigger, muon chamber efficinecy, the acceptance, the elastic definition,helicity distribution, proton dissociation, $\psi'$ contribtuion, luminosity give a contribution of ±15%. This was obtained as in [2].

## 10 Results

### 10.1 Photoproduction Cross Sections

The $J/\psi$ and $\Upsilon$'s elastic electroproduction cross section were calculated as:

$$\sigma(e^+p \to e^+Vp) = \frac{N_{evt}}{\mathcal{A}\ \mathcal{L}\ \mathcal{B}}, \tag{22}$$

where V stands for either $J/\psi$ or $\Upsilon$, $N_{evt}$ denotes the background subtracted number of V signal events, $\mathcal{A}$ the acceptance, $\mathcal{L}$ the integrated luminosity and $\mathcal{B}$ the leptonic branching fraction. For the $J/\psi$ $\mathcal{B}$ was set to $(6.01 \pm 0.19)\%$ [15]; for the $\Upsilon$'s the value of $(2.48 \pm 0.07)\%$ was used.
The photoproduction cross section is related to the $ep$ cross section by [23]

$$\sigma_{\gamma p\to Vp} = \frac{\int_{y_{min}}^{y_{max}}\int_{Q^2_{min}(y)}^{Q^2_{max}} \Phi(y,Q^2)\sigma_{\gamma p\to Vp}(y,Q^2)dydQ^2}{\Phi_T} = \frac{\sigma_{e^+p\to e^+Vp}}{\Phi_T}, \tag{23}$$

where $\sigma_{\gamma p\to Vp}$ is the mean cross section in the measured range of $W$ (corresponding to the limits $y_{min}$, $y_{max}$) and $Q^2$. The effective flux, $\Phi_T$, of virtual photons from the positron is computed as:

$$\Phi_T = \int_{y_{min}}^{y_{max}}\int_{Q^2_{min}(y)}^{Q^2_{max}} \Phi(y,Q^2)dydQ^2 = \int_{y_{min}}^{y_{max}}\int_{Q^2_{min}(y)}^{Q^2_{max}} \frac{\alpha}{2\pi yQ^2}[1+(1-y)^2-\frac{2M_e^2y^2}{Q^2}]dydQ^2, \tag{24}$$

where $\alpha$ is the electromagnetic coupling constant. The integrals run from $Q^2_{min} = M_e^2\frac{y^2}{1-y}$ to $Q^2_{max} = 3$ GeV$^2$ and from $y_{min} = W^2_{min}/s$ to $y_{max} = W^2_{max}/s$ where $W_{min}$ and $W_{max}$ are the minimum and maximum values of $W$, respectively, in each chosen interval.
The $J/\psi$ and $\Upsilon$'s electro- and photoproduction cross sections are summarized in Tab. 4. The first error is statistical and the second comes from adding in quadrature all the systematic errors described in section 9.
In Fig.30(a),(b) the photoproduction cross sections are compared with the predictions of [21] for different parametrizations of the proton structure function and with an early prediction of



B.Diekmann et al. for W=100 GeV [17]. Fig.31(a) shows the ratio of the cross sections as a function of W in the range where both can be measured. The ratio is constant within errors and indicates that the W dependence of the $\Upsilon$ cross section on W is similar to that of the $J/\psi$ and steeper than that found for the lighter vector mesons. Its value is $(1.1 \pm 0.4\ stat\ ^{+0.2}_{-0.4}\ syst)$ %. The data are consistent with the prediction of Diekmann [17]. The model of [21] would require $\approx 6$ events in the $\Upsilon$ region against the 32 ± 10 detected. A compilation of vector mesons cross-sections is shown in Fig. 31(b).
The $\psi(2S)/J/\psi$ ratio has been computed from the number of events quoted in 4, the ratio of the acceptances computed by MC and the PDG branching ratios [15]. It is found to be 0.17 ± .04 in good agreement with the recently published H1 [22] and previous results. The error is dominated by that on the branching ratio.

## 11 Conclusion

Using the ZEUS detector at HERA the cross section for elastic $\Upsilon$ photoproduction as well as its ratio to the $J/\psi$ 's has been measured for the first time and compared with some phenomenological predictions. The data suggest a similar dependence on the the photon-proton centre of mass energy for the two heavy vector mesons, steeper than for the lighter ones. A measurement of the $\psi(2S)/J/\psi$ ratio has also been performed and found in agreement with the value found in previous experiments.

## References

[1] ZEUS Collab., M. Derrick et al., Phys. Lett. **B350** (1995) 120.

[2] ZEUS Collab., J. Breitweg et al., Z. Phys. **C75** (1997) 215.

[3] H1 Collab., T. Ahmed et al., Phys. Lett. **B338** (1994) 507.

[4] ZEUS Collab., M. Derrick et al., Phys. Lett. **B356** (1995) 601.

[5] H1 Collab., S. Aid et al., Nucl. Phys. **B468** (1996) 3;
H1 Collab., S. Aid et al., Nucl. Phys. **B472** (1996) 3.

[6] M.G. Ryskin, Z. Phys C57 (1993) 89.

[7] E.L. Berger and D. Jones, Phys. Rev. **D23** (1981) 1521.

[8] F. Jacquet and A. Blondel, Proceedings of the Srudy of an ep Facility for Europe, DESY-79/48 (1979), U. Amaldi ed.

[9] S.P. Baranov et el., Physics at HERA, Vol.3, p.1478

[10] J.A.M. Vermaseren, Nucl.Phys., B229 (1983) p.347

[11] O. Dünger, Interner Bericht DESY F11/F22-94-01, 15

[12] B.H.Y. Hung et al., ZEUS-Note 95-013

[13] M. Arneodo, L. Lamberti and M.G. Ryskin, submitted to Comp. Phys. Comm. (1995).



| J/$\psi$ | $\langle W\rangle$ | $N_{Sig}$ | $\mathcal{A}$ | $\sigma_{ep\to eVp}$ (nb) | $\Phi_T$ | $\sigma_{\gamma p\to Vp}$ (nb) |
|---|---|---|---|---|---|---|
| | 50 | 1235 ± 35 | 0.19 | 1.74 ± 0.27 | 0.0392 | 44.34 ± 6.99 |
| | 70 | 1500 ± 40 | 0.30 | 1.31 ± 0.20 | 0.0253 | 51.63 ± 8.08 |
| | 90 | 1605 ± 40 | 0.38 | 1.11 ± 0.17 | 0.0179 | 61.80 ± 9.66 |
| | 110 | 1180 ± 35 | 0.29 | 1.05 ± 0.17 | 0.0134 | 78.04 ± 12.38 |
| | 130 | 675 ± 25 | 0.17 | 1.05 ± 0.17 | 0.0103 | 101.32 ± 16.74 |
| | 150 | 185 ± 15 | 0.05 | 1.01 ± 0.20 | 0.0081 | 124.98 ± 25.21 |
| $\Upsilon$ | $\langle W\rangle$ | $N_{Sig}$ | $\mathcal{A}$ | $\sigma_{ep\to eVp}$ (pb) | $\Phi_T$ | $\sigma_{\gamma p\to Vp}$ (pb) |
| | 100 | 11 ± 5 | 0.39 | $17.9 \pm 11.9^{+4.2}_{-7.3}$ | 0.031 | $570 \pm 380^{+134}_{-231}$ |
| | 140 | 11 ± 5 | 0.41 | $17.1 \pm 11.4^{+6.9}_{-4.0}$ | 0.0184 | $926 \pm 618^{+217}_{-375}$ |

Table 4: The results for the integrated $J/\psi$ and $\Upsilon$ photoproduction cross section as a function of $W$. $N_{Sig}$ is the number of events after subtraction of the Bethe-Heitler contribution and $\mathcal{A}$ is the acceptance. The photon flux $\Phi_T$ is calculated as described in the text and used to calculate the $\gamma p$ cross section, $\sigma_{\gamma p\to Vp}$, from the $ep$ cross section, $\sigma_{ep\to eVp}$, where V means $J/\psi$ or $\Upsilon$ as appropriate. Cross sections for $J/\psi$ are quoted with the the total error only, the statistical one being negligible. For the $\Upsilon$ the first error is statistical and the second systematic.

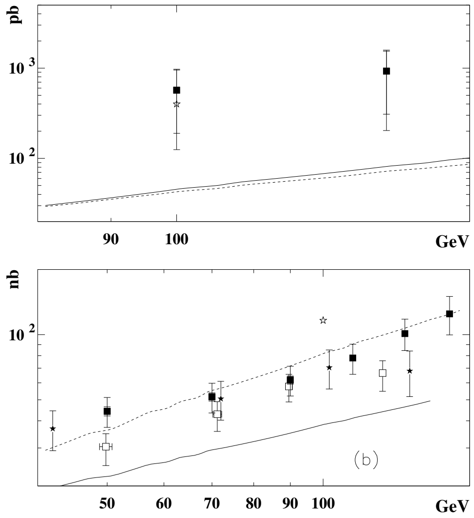


Figure 30: Photoproduction Cross Section for $\Upsilon$ (a) and $J/\psi$ (b), as a function of W, the centre of mass energy of the photon-proton system. Data (full squares) are compared with H1 (black stars) and ZEUS (open squares) published data and with the predictions of Diekmann [19] (open star) and of [21] for the GRV94(HO) (dashed line) and MRS(R2) (full line) parametrizations of the proton structure function.



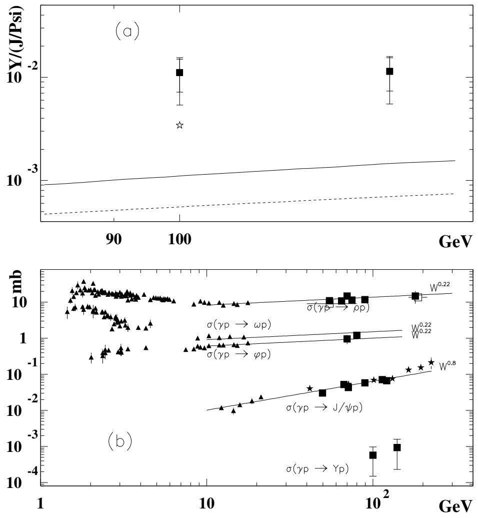


Figure 31: (a) $\Upsilon/J/\psi$ ratio as a function of W, the centre of mass energy of the photon-proton system. Data (full squares) are compared with the predictions of Diekmann [19] (open star) and of [21] for the GRV94(HO) (dashed line) and MRS(R2) (full line) parametrizations of the proton structure function. In (b) the $\Upsilon$ data of this paper are compared with a compilation of published results for other vector mesons.



[14] M. Kasprzak, EPSOFT, Zeus-Note 95-069.

[15] Particle Data Group, L. Montanet et al., Phys. Rev. D50(3)(1994) 1173.

[16] S. W. Herb et al., Phys. Rev. Lett. **39** (1977) 252.

[17] J.H.Cobb et al., Phys. Lett. **B72** (1977) 273;
Ueno et al., Phys. Rev. Lett. **42** (1979) 486;
J.Badier et al., Phys. Lett. **B86** (1979) 98;
C.Kourkoumelis et al., Phys. Lett. **B91** (1980) 481;
NA10 Collab., Phys. Lett. **B158** (1985) 92;
NA10 Collab., Phys. Lett. **B179** (1986) 170;
CDF Collab., Phys. Rev. Lett. **75** (1995) 4358;
E771 Collab., Phys. Lett. **B374** (1996) 271 .

[18] BCDMDS Collab., Nucl. Phys. **B199** (1982) 27;
EMC Collab., Nucl. Phys. **B213** (1983) 1.

[19] B.Diekmann et al., Proc. of the HERA Workshop (1987) 515;
M.G. Ryskin, Z. Phys. **C57** (1993) 89;
L.Frankfurt et al., hep-ph/9702216v3.

[20] M. Strikman, private communication.

[21] R. Engel, based on L. Frankfurt et al. , private communication.

[22] H1 Collab., C. Adloff et al., DESY 97-228.

[23] V.N. Gribov et al., Sov. Phys. JETP 14 (1962) 1308;
V.M. Budnev et al., Phys. Rep. C15 (1975) 181.

[24] *http : //www − zeus.desy.de/ bellagam/ZEUS_ONLY/ups/upsnew_1.html*